

Article

Integration of RUSLE Model, Remote Sensing and GIS Techniques for Assessing Soil Erosion Hazards in Arid Zones

Elsayed A. Abdelsamie¹, Mostafa A. Abdellatif¹, Farag O. Hassan¹, Ahmed A. El Baroudy² ,
Elsayed Said Mohamed^{1,3} , Dmitry E. Kucher³  and Mohamed S. Shokr^{2,*} 

¹ National Authority for Remote Sensing and Space Sciences, Cairo 11843, Egypt

² Soil and Water Department, Faculty of Agriculture, Tanta University, Tanta 31527, Egypt

³ Department of Environmental Management, Institute of Environmental Engineering, People's Friendship University of Russia (RUDN University), 6 Miklukho-Maklaya Street, 117198 Moscow, Russia

* Correspondence: mohamed_shokr@agr.tanta.edu.eg

Abstract: Soil erosion constitutes one of the main environmental and food security threats, derived from the loss of its productive capacity. With the help of remote sensing (RS), geographic information systems (GIS), and a revised version of the universal soil loss equation (RUSLE), this research has mostly focused on measuring the potential soil erosion hazard and soil water conservation ratio (SWCR) in the El-Minia region of Egypt. Based on the integration of S2A images and the digital elevation model (DEM), geomorphological units of the study area were identified. The RUSLE model includes parameters that allow for mapping soil erosion, such as rain erosivity, soil erodibility, slope length and steepness, soil cover and management, and soil conservation practices. The outcomes revealed that the classes of annual erosion rates of the study area are those of "slight erosion", "low erosion", "moderate erosion" and "moderately high erosion", which represent percentages of 29%, 18%, 33% and 20%, respectively, of the total area. The rate of erosion decreases from east to west. The main erosion factors in the research area are the low vegetation cover and the high slope values. This study highlights the utility of combining the classic RUSLE equation with techniques such as remote sensing (RS) and geographic information systems (GIS) as a basis for assessing current erosion conditions in arid environments and, specifically, for the application of soil management patterns aimed at increasing soil organic matter and any other soil conservation actions. The findings of this study can be used by policymakers to implement soil conservation measures if development projects are to proceed in areas with a high risk of soil erosion. The approach described here is therefore adaptable to similar environments in arid regions.

Keywords: soil erosion modeling; revised universal soil loss equation; dryland region; remote sensing; GIS



Citation: Abdelsamie, E.A.; Abdellatif, M.A.; Hassan, F.O.; El Baroudy, A.A.; Mohamed, E.S.; Kucher, D.E.; Shokr, M.S. Integration of RUSLE Model, Remote Sensing and GIS Techniques for Assessing Soil Erosion Hazards in Arid Zones. *Agriculture* **2023**, *13*, 35. <https://doi.org/10.3390/agriculture13010035>

Academic Editors: Manuel Rodríguez-Rastrero, Alicia Palacios-Orueta and Ryusuke Hatano

Received: 9 October 2022

Revised: 3 December 2022

Accepted: 21 December 2022

Published: 22 December 2022



Copyright: © 2022 by the authors. Licensee MDPI, Basel, Switzerland. This article is an open access article distributed under the terms and conditions of the Creative Commons Attribution (CC BY) license (<https://creativecommons.org/licenses/by/4.0/>).

1. Introduction

Soils are considered a crucial component of the Earth's surface, as they facilitate the provision of vital ecosystem services [1,2]. Healthy soil is required in the 21st century for human requirements such as high-quality water, clean air, and food [3]. Soil erosion is the process through which soil material is lost due to the action of wind and water, widely caused by human activity [4,5]. Additionally, soil erosion caused by human activity has negative consequences on the environment and the economy [6]. One of the most serious environmental issues in the world is soil erosion [6], which can lead to a number of issues related to land degradation, such as a decrease in soil mass and water quality and an increase in river sedimentation [7]. Environmental stressors and human activities may cause soil degradation [1]. Among the factors that affect erosion worldwide, associated with the increase in population, is the expansion of agricultural land, with consequent deforestation and overgrazing [8]. Erosion can destroy the land, which may contain fewer

plants capable of absorbing the carbon dioxide that warms the climate [6]. Soils can store enough greenhouse gases in a year to equal approximately 5% of annual human-made greenhouse gas emissions [9].

Each year, 10 million hectares (ha) of croplands are lost due to soil erosion [6]. Because soil erosion influences biogeochemical cycles, it interacts with climate change itself [10,11]. As a result, the effects of climate change in drylands require increased attention [12]. In these regions, soil erosion is linked with agriculture, and some of these problems are loss of fertile topsoil for agriculture and a decrease in soil productivity and agricultural sustainability [13,14]. Egypt suffers from a shortage of water, which influences agricultural production and increases the gap between the production of food and consumption due to continuing population growth [15]. Scientists have used several methods to assess soil erosion [16]. Spatial distribution and models for quantifying soil loss in the field are costly; in addition, time-consuming and insufficient sample plots might impair the regularity of the real spatial degree of the areas suffering erosion [17,18]. Soil erosion losses have been assessed by several studies all over the world using RS and GIS techniques [19–21]. These studies have demonstrated that land use changes are affected directly by annual soil loss [6]. However, some studies have found that human impact on dynamic changes in sediment output is more critical than climate change [22].

Satellites equipped with remote sensors can provide frequent images over specific and wide regions. Furthermore, the quick development of suitable indices can significantly contribute to the assessment of regional soil erosion risk [23]. As for quality in terms of spatial and temporal resolution, Landsat data have been freely accessible since the early 1970s, which greatly increased their use among researchers [24,25]. The European Space Agency's latest release of multispectral satellite SENTINEL-2A data (S2A) in November 2015 was groundbreaking for creating images of vast areas with a 290 km-wide width at high revisit frequency [26]. The S2A's better spatial resolution enables more accurate mapping of both smaller and bigger disturbances in comparison to Landsat 8 OLI [27]. Concerning land use and land cover classification, S2A images are more accurate than those from Landsat 8 [28], and S2A generated vegetation indices produced better prediction accuracy [29]. In order to incorporate spatiotemporal fluctuations in cover factor (C) determination for erosion prediction on a broader landscape scale, the normalized difference vegetation index (NDVI) has become increasingly popular [30]. The accurate application of atmospheric correction techniques is essential and has a big impact on NDVI estimates. Fast line-of-sight atmospheric analysis of hypercubes (FLAASH) created the NDVI raster with the greatest degree of distinctness [31]. Among the most-used NDVI modifications in soil erosion research are the soil adjusted vegetation index (SAVI) created by [32] and the soil and atmospheric resistant vegetation index (SARVI) proposed by [33].

The soil loss equation (USLE) and the revised universal soil loss equation (RUSLE) are two models that have been used to evaluate soil loss [16,34]. Numerous researchers have utilized erosion models in conjunction with RS tools and GIS [35–37] to raise the accuracy of erosion assessments and predictions of soil erosion risk on spatial maps [6]. The empirical equation of RUSLE is the best procedure for assessing soil erosion [38–40] due to its low data requirements and simple structure. This is very useful in developing countries, as the implementation of complicated models may be restricted by a deficiency of acceptable input data [41]. However, there are some published studies on the implementation of remote sensing and GIS techniques in other areas of the world [42].

On the other hand, the El-Minia region of Egypt lacks previous research based on the combination of GIS and RS to model soil erosion. This work proposes that, in order to evaluate the erosion conditions in such an arid region, the use of a “traditional” technique based on a widely tested equation combined with techniques in full development like GIS and RS can be generally applied in other arid areas.

In accordance with the above, the objectives of this work are the following: on the one hand, to measure the potential for soil erosion in an arid climate region, and on the other, to calculate the SWCR index to quantify water conservation and soil conditions in the

research area. These general objectives of the study require the following specific objectives: (a) identify the geomorphological units of the study area; (b) establish a method to evaluate the spatial variation of soil erosion within the study area by combining RS, GIS, and the RUSLE equation; (c) produce a final synthetic map, highlighting the areas of high and low erosion.

The results of this study can provide decision-makers with accurate data that can be useful in planning, land management strategies, and soil restoration for sustainable agriculture. In addition, this model can be applied in the same way in other arid areas to achieve the same objectives.

2. Materials and Methods

2.1. Experimental Area

This area is located in the middle of the Nile Valley (Figure 1). It occupies an area of 70,981 ha. The coordinates of the area under research are 30°30'00" and 30°49'00" longitude and 28°00'00" and 28°21'0" latitude. The highest elevation within the study area is about 153 m above sea level (m.a.s.l). The investigated area is categorized by arid climate, as the summer is hot and the winter is warm, while the rain intensity is low; in addition, the evaporation rate is high. The warmest months are June–August, as the average temperature could reach 30.2 °C. December–February is the coldest period of the year, as the average temperature is 12.9 °C according to the meteorological station of the El-Minia governorate (EMA, 2020). The total average precipitation is around 28 mL year⁻¹ [43]. Southern parts of the study area received wastes produced by the Abu Qurqas sugar plant for about 100 years; in addition, the area under investigation contains alluvial deposits [44].

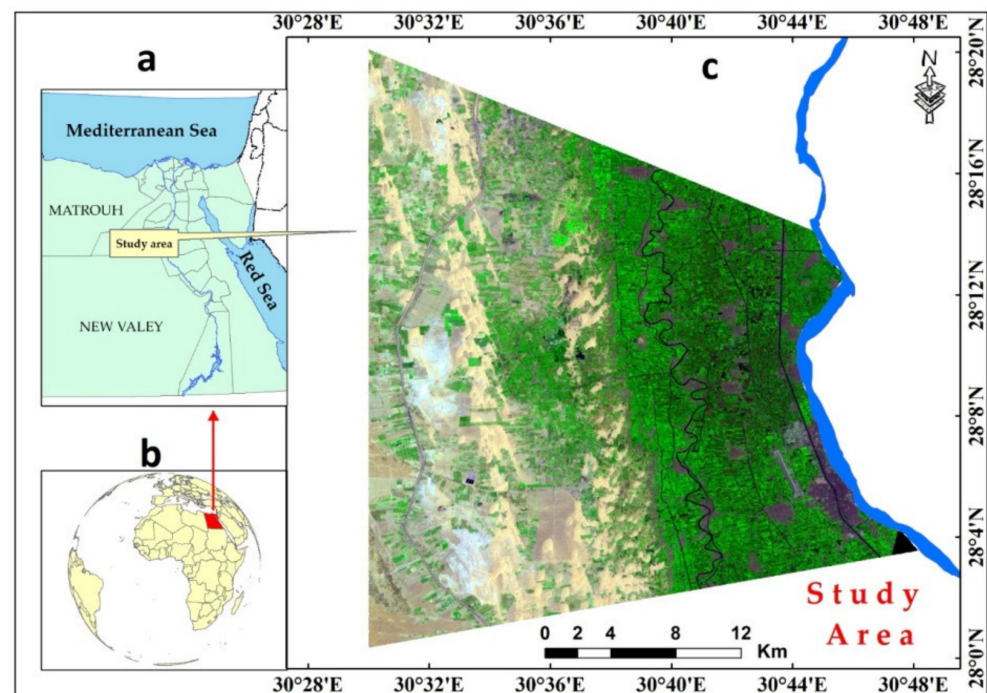


Figure 1. (a) Location of Egypt on the world map, (b) map of Egypt (c) location of area under investigation (b).

The following flow chart (Figure 2) provides a summary of the current work's procedure:

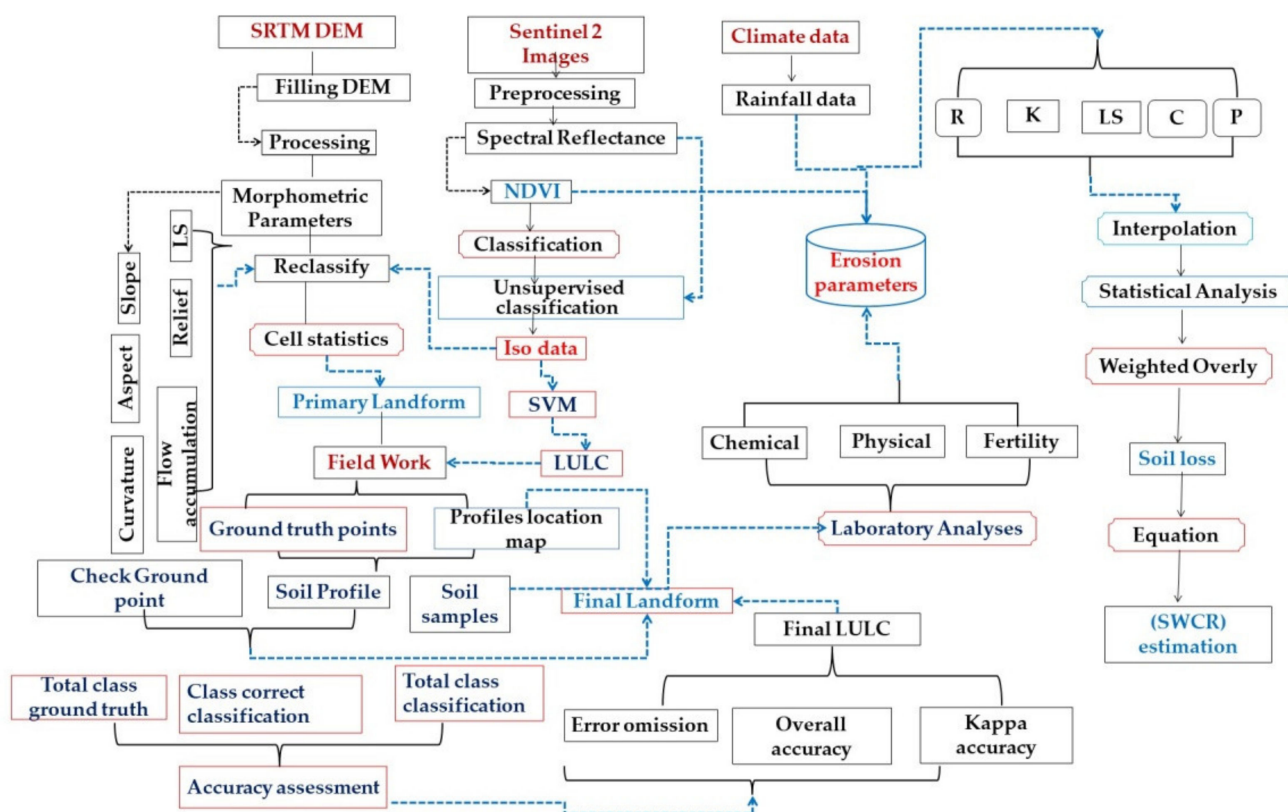


Figure 2. Current work methodology schematic chart.

2.2. RS Data

Using 13 spectral bands of the MSI (multispectral imager) instrument with 4 bands at 10 m, 6 bands at 20 m, and 3 bands at 60 m spatial resolution, the S2A satellite images from the ESA (European Space Agency) provided high-resolution multi-spectral optical imagery [45]. The FLAASH model was used to atmospherically adjust S2 data utilizing ENVI 5.3. FLAASH is a cloud detection and atmospheric correction technique [46–48]. The satellite image that was downloaded from <https://www.usgs.gov> (accessed on 16 August 2021) was already geo-registered to the position indicated by the WGS 1984 UTM Zone 36 N. All spectral bands were resampled to 10-m resolution by SNAP software [49]. Sentinel 2 was used to differentiate between different types of land use and cover (LU/LC). ISO data classification was used for unsupervised classification. Unsupervised categorization is frequently referred to as clustering since it relies on the natural groupings of pixels in image data [50]. The support vector machines (SVM) approach was used to extract LU/LC, which enables the separation of classes with a decision surface that maximizes the margin between the classes, producing accurate classification results from complicated and noisy data [51]. Although the supervised categorization approach takes more time, it produces findings that are more generally correct than the unsupervised categorization method [52]. To evaluate the outcomes and decide on the most effective method for classifying LU/LC, overall accuracy, kappa analysis, and emission errors were calculated using the same reference points for the S2A and Landsat OLI 8 classifications.

2.3. Geomorphological Analysis

SENTINEL 2A (S2A) satellite spectral information (16 August 2021), United States Geological Survey (USGS), topographic data, and field surveys were included as input data to extract landform units [53]. A digital elevation model (DEM) with 30 m resolution corrected by applying the Planchon and Darboux algorithms [54] (Figure 3) was used to derive topographic indices such as slope, aspect, curvature, and hill shading using SAGA GIS software. In particular, on the transition zones between the classes of the DEM, the

reclassified parameters had a mixture of stand-alone and small contiguous areas. To reduce mistakes and noise, a simple filter based on focus neighborhood statistics was employed. The focal neighborhood statistics were used to apply a filter to the parameters layers to solve this issue. The most prevalent value within the targeted neighborhood was chosen as the center pixel of the moving window for the majority focus statistic. The center pixel of the moving window was given the average value of the specified neighborhood pixels for the mean focal statistic [55]. Using field checkpoints and previous research, we can recognize the landform units based on S2A optical interpretation and DEM in 3D display mode.

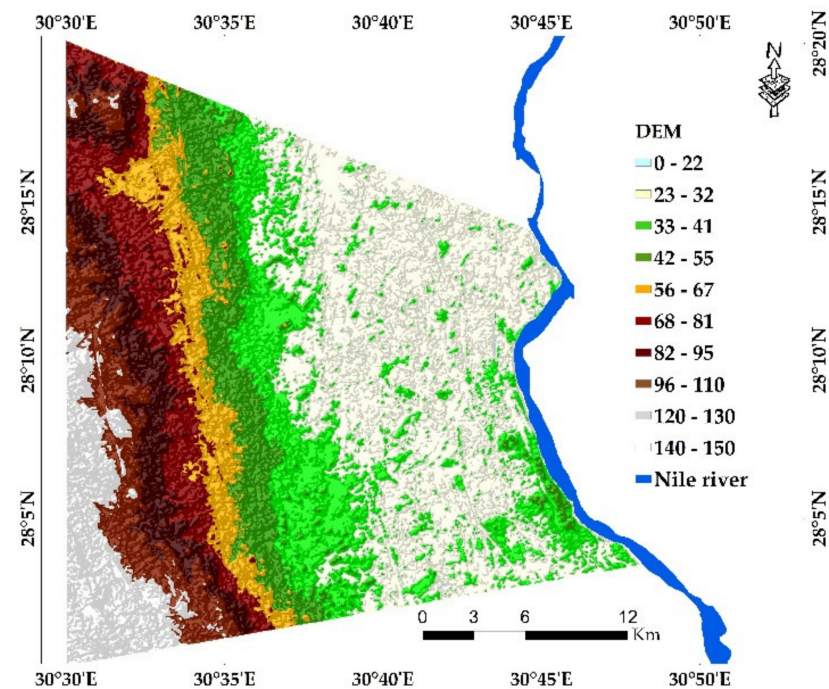


Figure 3. Digital elevation model (DEM) of area under investigation.

2.4. Soil Sampling and Laboratory Analysis

Thirty-two soil profiles were chosen to represent the different landforms and landscape units within the study area. Description of the morphological features and soil classification were done according to [56,57], respectively. The depths of soil profiles differ between 80 to 150 cm depending on the presence of a water table or bedrock. Physical, chemical, and fertility characteristics of soil samples were analyzed in an accredited soil, water, and plant laboratory according to ISO/IEC 17025 (2017) requirements at the Faculty of Agriculture, Tanta University. Chemical analysis included such as soil salinity (EC), soil pH, percentage of calcium carbonate ($\text{CaCO}_3\%$), cation exchange capacity (CEC), and exchangeable sodium percentage (ESP), as well as fertility analysis, including soil organic matter (SOM%) and available nitrogen (N) using the Kjeldahl method, phosphorus (P) and potassium (K), while physical analysis included particle size distribution [58–62].

2.5. Soil Erosion Modeling

The RUSLE model is utilized in the current study to estimate the average soil loss, as it is a predictive empirical model that is utilized commonly to estimate the average annual soil loss based on computing the parameters of soil erosion [16]. It is developed from the USLE model [63]. The erosion of soil by water was estimated through the integration of S2A, DEM, and a dataset of rainfall and soil data. The following Equation (1) describes the steps of soil loss calculation by RUSLE.

$$A = R \times K \times LS \times C \times P \quad (1)$$

where:

A = average annual soil loss ($\text{Mg ha}^{-1} \text{ year}^{-1}$)

R = denotes the erosivity factor due to the density of rainfall ($\text{MJ} \cdot \text{mm ha}^{-1} \text{ h}^{-1} \text{ year}^{-1}$)

K = refers to soil erodibility, ($\text{Mg m}^2 \text{ h ha}^{-1} \text{ hJ}^{-1} \text{ cm}^{-1}$)

LS = L refers to slope length factor, while S refers to slope steepness

C and P = cover management and supporting practice factors, respectively

LS, C, and P are all dimensionless factors [16].

2.5.1. Erosivity by Rainfall (R)

This is the most relevant factor in the RUSLE model in the context of climate change because it depicts the extent of soil erosion caused by rainfall intensity, which is crucial for assessing the risk of soil erosion under future changes in land use and climate [64,65]. The present erosivity index was calculated utilizing mean rainfall data collected from the meteorological station of the El-Minia governorate. Analytical variety equations are implemented to assess R factors based on rainfall totals. R values were estimated as given in Equations (2) and (3) according to [66] as the following:

$$R = 0.07397 \times (F \times 1.847)^{1.72} \quad (2)$$

$$F = \sum^{12} (pm)^2 / P \quad (3)$$

where:

F = the modified Fournier coefficient

Pm = the precipitation/month

P = the precipitation/year (mm)

2.5.2. Soil Erodibility Factor (K Factor)

This factor is the soil's physical and chemical property interaction that influences detachment, transportation, and capacity of infiltration. The most important determinants of erodibility are soil structure, texture, SOM%, and permeability [63,67]. Thus, the aforementioned parameters have been utilized to estimate the erodibility of the soil, which ranges from 0–1 (Equation (4)) [68].

$$k = 2.11 \times 10^6 (12 - \text{SOM}\%) \times (M)^{1.14} + 0.325 \times (S - 2) + 0.025(P - 3) \quad (4)$$

where:

M = (silt + very fine sand) (100-clay),

S and P = structure and permeability factors, respectively

2.5.3. Slope Length and Steepness Length (LS) Factor

This factor S shows the impact of topographic features on soil erosion as it considers the topographic aspect of a specific area for erosion. Equation (5) was implemented using the raster calculator function in SNAP software to calculate the LS factor. The topographic properties of the study area (DEM, slope, aspect, and flow accumulation) are demonstrated in Figure 4).

$$LS = \frac{(\text{flow accumulation} \times \text{cell size})^{0.4}}{22.13} \times \left(\frac{\sin \text{slope}}{0.0896} \right)^{1.3} \quad (5)$$

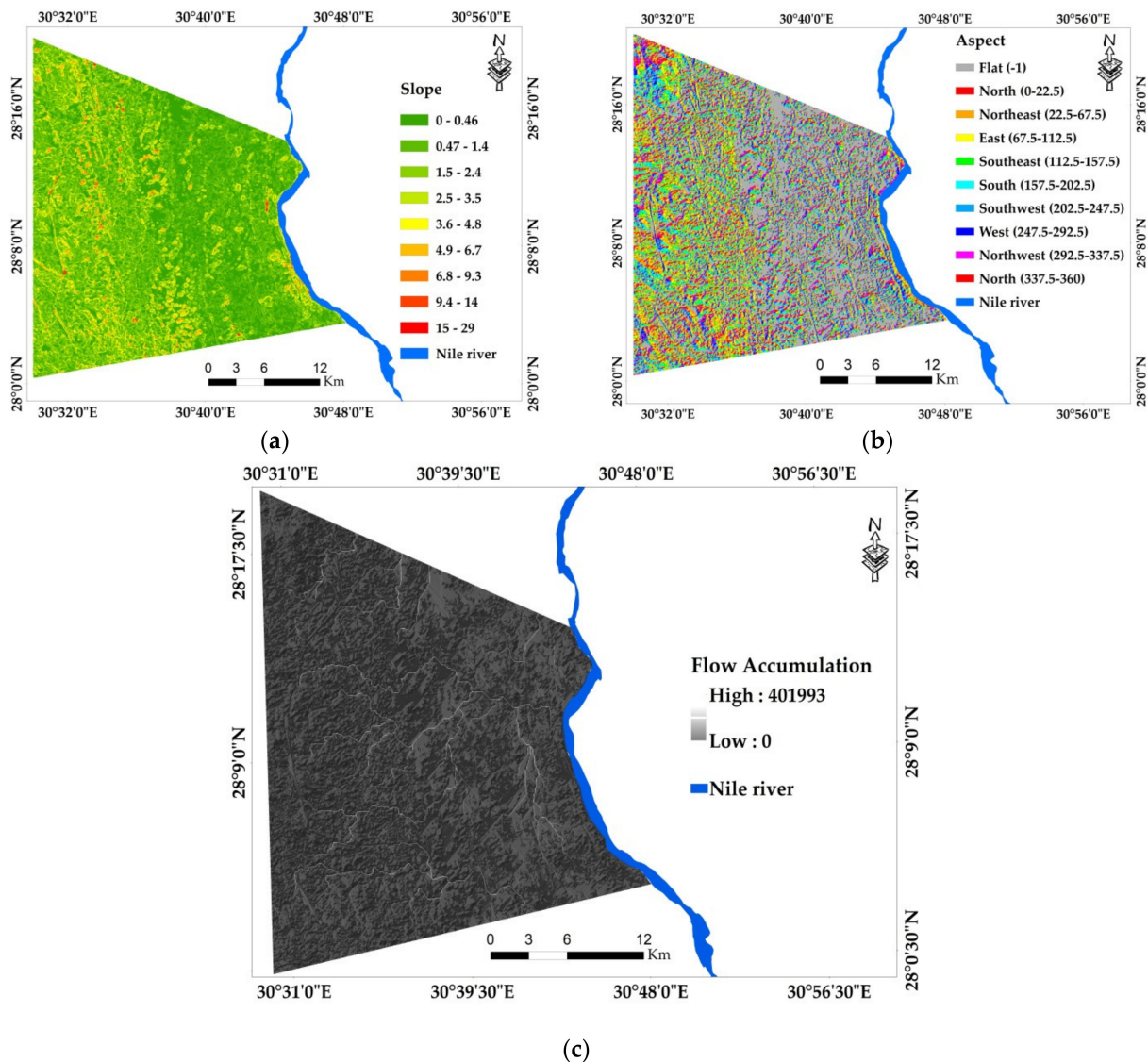


Figure 4. Maps of (a) the slope, (b) the aspect, and (c) the flow accumulation.

2.5.4. C Factor

Different practices of soil management can significantly prevent the soil from eroding by decreasing the surface runoff velocity, reducing intensity of raindrops that hit the soil surface, and preventing its disturbing action [69]. Values of C factor were calculated according to Equation (6) and relied on the normalized vegetation cover index values (NDVI), which were extracted from the S2A image.

$$C = (1 - \text{NDVI})/2 \quad (6)$$

The S2A satellite image (acquired on 16 August 2021) was utilized to extract values of NDVI. Based on red and near-infrared spectral reflectance data, Sentinel 2's normalized difference vegetation index (NDVI) was extracted, and 842 nm and 665 nm wavelength bands were used to derive the NDVI. Since the NDVI represented both human activity and the natural conditions of the study area, it was utilized to illustrate the regional variance of vegetation cover. The raster calculator tool in SNAP software was used to perform the following Equation (7) of NDVI [70].

$$\text{NDVI} = \frac{\text{NIR} - \text{IR}}{\text{NIR} + \text{IR}} \quad (7)$$

2.5.5. Support Practice Factor (P Factor)

This factor is the ratio between the soil loss in the field where a specific method of conservation is implemented and other fields without any conservation; in other words, it can measure the different practices of land management that decrease land degradation [16,71,72]. Because of the extent of the investigated area, soil and water conservation is not applied within the study area; thus, the value of the P factor is considered to be 1 [63].

2.6. Calculation of Soil and Water Conservation Ratio (SWCR)

The new evaluation index SWCR was suggested in 2019. This index has two possible values: the current value and the long-term target value. The current value of SWCR reflects the status of soil and water conservation in the study area. It was calculated as the following Equation (8) according to [73].

$$SWCR = SD \div TS \tag{8}$$

where:

SD is the area with a slight degree of erosion
 TS is total study area.

2.7. Mapping of Soil Properties

An advanced geostatistical procedure named ordinary kriging (OK) was used in the current study, as it can create non-stop surfaces from disturbed soil samples based on their properties [74]. Equation (9) of OK is as follows:

$$Z(x_0) = \sum_{i=1}^n \lambda_i(x_0)Z(x_i) \tag{9}$$

where:

$\sum \lambda_i = 1$ $\lambda_i(x_0)$ is equal to 1
 $Z(x_0)$ = the predicted value of variable z at location x_0
 $Z(x_i)$ = the measured data; $\lambda_i(x_0)$ refers to the weights linked with the measured values; and n is the number of predicted values within certain neighboring soil samples.

$$Y(h) = \begin{cases} C_0 + C \left(1 - \exp\left(-\frac{h^2}{a^2}\right) \right), & h > 0 \\ 0, & h = 0 \end{cases} \tag{10}$$

The spherical equation was identified as:

$$Y(h) = \begin{cases} C_0 + C \left(\frac{3h}{2a} - \frac{1}{2} - \left(\frac{h}{a}\right)^3 \right), & 0 < h \leq a \\ C_0 + C, & h > a \\ 0, & h = 0 \end{cases} \tag{11}$$

The circular equation was identified as

$$Y(h) = \begin{cases} C_0 + C \left(1 - \frac{2}{\pi} \cos^{-1} \frac{h}{a} + \sqrt{1 - \left(\frac{h}{a}\right)^2} \right), & 0 < h \leq a \\ C_0 + C, & h > a \\ 0, & h = 0 \end{cases} \tag{12}$$

In these above-mentioned Equations (10)–(12), a is the definite range for the spherical, circular, exponential, and Gaussian functions, respectively.

where:

h = the spatial lag,
 C_0 = the nugget, and

C = the partial sill.

3. Results and Discussion

3.1. Land Use (LU) and Land Cover (LC) of the Study Area

Figure 5 demonstrates the land use and land cover of the study area. Approximately 33,110 ha of the total area is bare soil; in contrast, 27,041.8 ha of the study area are agricultural lands, and 5832.64 ha and 4997.24 ha of the investigated area are classified as sand dunes and urban areas (housing structures and industrial zones), respectively. The main field crops in the summer season are soybean and maize; in addition, cotton is represented in scattered areas. These results are similar to [40]. In terms of classifying the study region, the errors of omission for the S2A image classification were 0.0% for bare soil and sand dunes, 1.5% for urban areas, and 11.82% for agricultural areas; they were, respectively, 0.15, 15.97, and 23.27% for the Landsat OLI 8 image classification for bare soil, urban, agriculture, and sand dunes. The S2A image, with an overall accuracy of 95.4%, outperforms Landsat OLI 8, with an overall accuracy of 89.4%, while S2A's kappa coefficient is 90.3%, and Landsat-8's is 82.9% (Table 1). Similar investigations demonstrated that Sentinel-2 outperforms Landsat-8; the better performance could be associated with red-edge-vegetation bands [75–77].

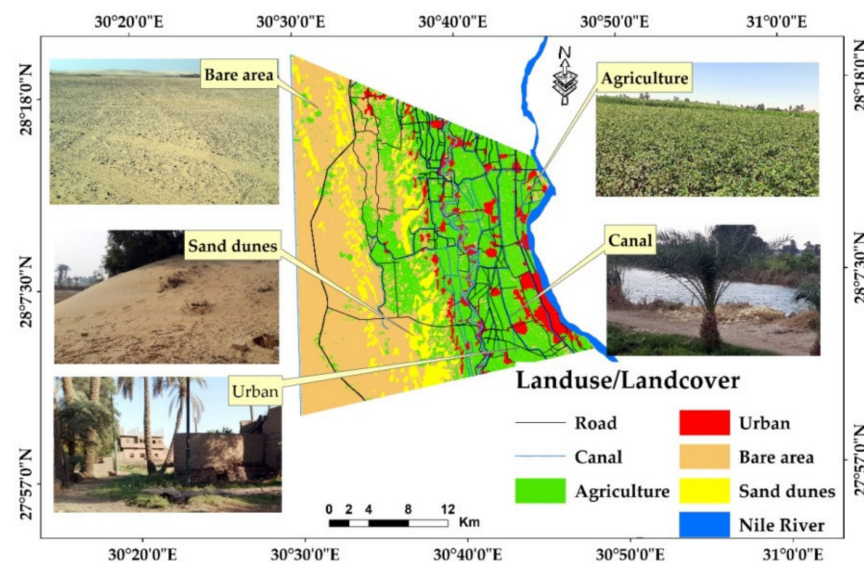


Figure 5. Land use and land cover of experimental area.

Table 1. Error of omission, kappa coefficient, and accuracy evaluation for the LU/LC of the study area based on SA and Landsat OLI 8.

Classes	Truth Points	Error of Omission %	
		S2A	OLI 8
Urban	66	1.50	1.50
Bare soils	149	0.00	0.00
Sand dunes	59	0.00	23.27
Agriculture	313	11.82	15.97
Overall accuracy		95.4	89.40
Kappa coefficient		90.30	82.90

3.2. Geomorphological Features of Investigated Area

From DEM and S2A, landform units were extracted, and the main landforms are shown in Figure 6. Decantation basins are formed on both sides of the river; these areas are characterized by low elevation and receive different sediments and water from the uplands that surround them [78]. They occupy about 14.2% of the investigated area, while overflow

basins cover around 6430 ha. The levee unit is an extended natural ridge regularly parallel to the river course bordering the alluvial plain [78], the area of this unit is about 0.80% of the total area. Dry valleys are very common in semiarid zones [79]; this unit covers around 0.17% of the total area. Old river terraces and recent river terraces are created from cyclic erosion and deposition stages of alluvial sediments [80] and cover an area of 18,625.2 ha (26.23%) and 7741.7 ha (10.9%) of the investigated area, respectively. River meandering belts were formed from deltaic plains deposited in the current age at the decantation basin's edges [81]. This unit covers an area of 1046.41 ha. Alluvial fan and outwash plains units occupy around 4.8% and shoulders 6.65% of the investigated area, respectively. Pediment units cover approximately 7% of the study area; the sediments of these units are transferred to basins or valley lowlands [82], while peneplain occupies 5153 ha of the area under study. Sand dunes, mesas, and rock outcrops represent 8.29%, 3.03%, and 0.05% of the total investigated area.

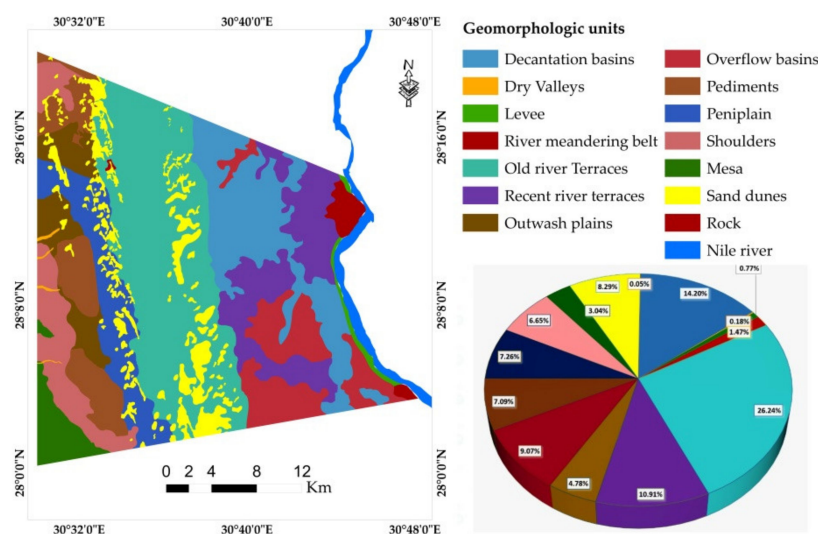


Figure 6. Geomorphologic units within the study area and a pie chart illustration of the percentage of their areas.

3.3. Relevant Soil Properties of the Study Area

Statistical analysis and interpolation maps of mean weighted soil properties are illustrated in Table 2 and Figure 7. The pH values fluctuated between 7.61 and 8.51 from west to east, which means that the study area is characterized as mildly/strongly alkaline. The SD of pH = 0.37 shows that there is a significant degree of pH similarity among the study area's various units [83]. It is known that soil pH has an impact on physical, chemical, and biological properties [84–86]. Since the EC values range from 0.18 to 10.38 dS m⁻¹, this region contains both non-saline and high-salinity soils. Due to arid conditions and high evaporation rates, the majority of salinized soils are found in drylands [87]. The SD of EC is equal to 3.14, indicating that this property varies widely within the study area, and it was observed that it increased from the east to the west of the study area. High-quality water is required for leaching high-salinity soils [88,89]. The CaCO₃% values show a wide range from 1.05% to 59.16%; the highest values are associated with the presence of parent materials rich in shell fragments. High variations of CaCO₃% were noted within the study area as SD > 14. The SOM% content of the study area fluctuated between 0.01 and 1.33%, and it increased in the east of the study area as areas close to the Nile River are more fertile. These results agree with the arid condition of the study area, which determines a very limited contribution of organic matter to the soil [83]. The CEC varies from 3.57 to 47.7 cmol + kg⁻¹; these values are associated with clay and SOM% content [90]. The ESP content varies from 7.69 to 24.76%, with a weighted mean of 13.32. The high content of ESP can negatively affect soil structure and hydrology, which leads to a decrease

in crop productivity [91]. The available N, P, and K ranged from 3.1–31.5, 3.10–12.6, and 39–417 mg Kg⁻¹ with SD = 9.71, 2.07, and 120.58, respectively, and they increased gradually to the east of the study area where the Nile River is located. The low values of macronutrients may be due to high values of pH and low vegetation over the study area.

Table 2. Statistics of some mean weighted soil properties.

Soil Properties	EC dS m ⁻¹	pH	CaCO ₃ %	SOM%	CEC cmolc Kg ⁻¹	ESP	N mg kg ⁻¹	P mg kg ⁻¹	K mg kg ⁻¹
Min	0.18	7.61	1.05	0.01	3.57	7.69	3.10	3.10	39.00
Max	10.38	8.51	59.16	1.33	47.69	24.76	31.50	12.60	417.00
Average	3.46	7.99	13.67	0.48	20.26	13.32	18.15	7.02	240.59
SD	3.41	0.27	14.10	0.47	12.23	5.56	9.71	2.07	120.58

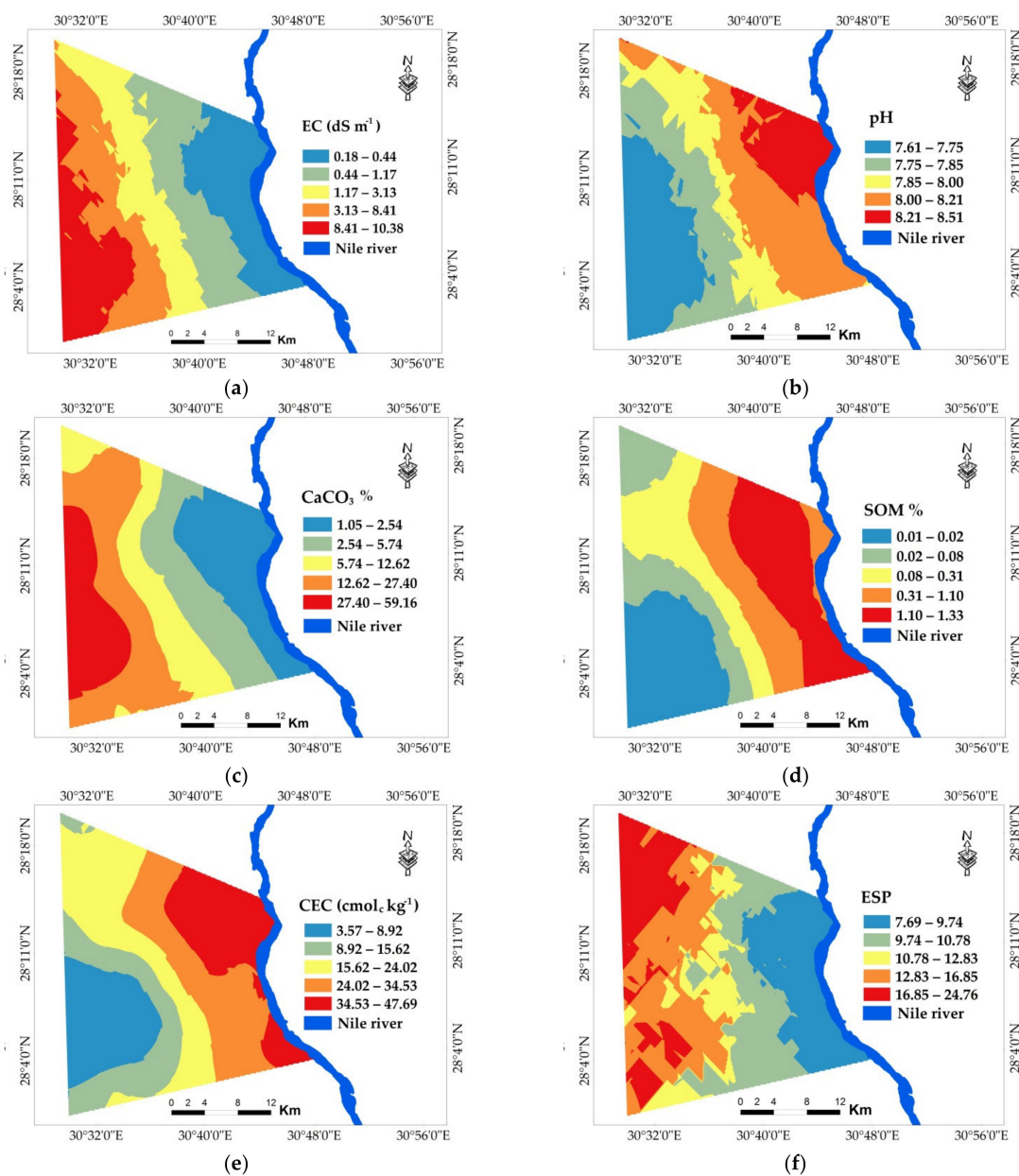


Figure 7. Cont.

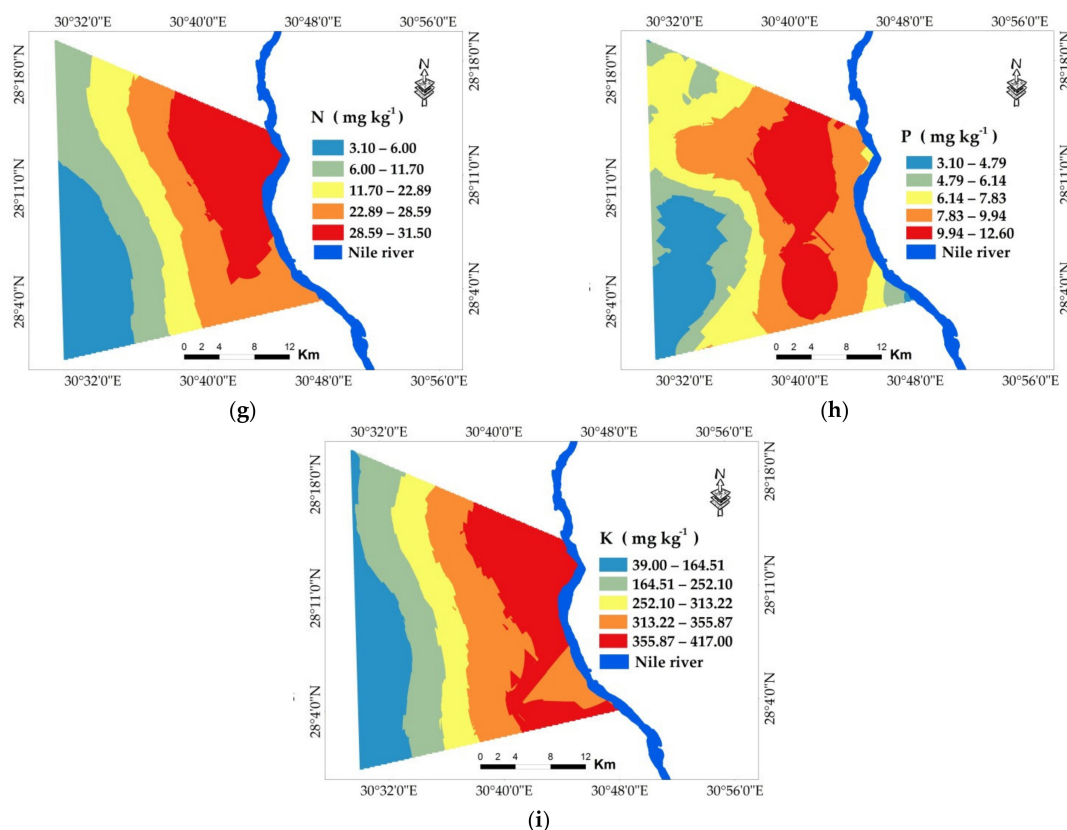


Figure 7. Interpolated maps of some mean weighted soil properties: (a) soil salinity (EC dSm⁻¹), (b) soil reaction (pH), (c) % of calcium carbonate (CaCO₃%), (d) % soil organic matter (% SOM%), (e) cation exchange capacity (CEC cmolc+ kg⁻¹), (f) exchangeable sodium percent, (g) average nitrogen (N mgkg⁻¹), (h) average phosphorous(mg kg⁻¹), and (i) average potassium (mg kg⁻¹).

3.4. Spatial Distribution Accuracy of Soil Properties

As can be seen in Table 3, the accuracy of each model was confirmed by calculation of mean standardized error (MSE), root mean square error (RMSE), and root mean square standardized error (RMSSE). The results showed that the Gaussian model is suitable for EC, ESP, SOM, P, and K, while the spherical model is the best one for pH CaCO₃%; lastly, the circular model is more appropriate for CEC and N. The above-mentioned models are the most suitable models for predicting the unsampled sites due to MSE and RMSSE 0 and 1, respectively [92–94].

Table 3. Accuracy of geostatistical OK analysis of soil properties.

Soil Parameters	Model Type	Mean	RMSE	MSE	RMSSE
EC (dS m ⁻¹)	Gaussian	−0.08	3.14	0.02	0.95
pH	Spherical	0.01	0.27	0.04	1.02
CaCO ₃ %	Spherical	0.020	12.78	0.00	1.01
SOM%	Gaussian	0.01	0.38	0.01	1.08
CEC (cmolc/kg)	Circular	0.00	11.17	0.00	0.99
ESP	Gaussian	−0.16	5.42	−0.02	0.97
N (mg kg ⁻¹)	Circular	0.07	7.61	0.00	0.96
P(mg kg ⁻¹)	Gaussian	0.23	1.87	0.09	0.96
K (mg kg ⁻¹)	Gaussian	−1.04	90.93	−0.01	0.99

3.5. Soil Erosion Calculation by RUSLE

Erosion factors are illustrated in Figure 8. The K values of soils that have high amounts of clay are low because of separation resistance, as sandy soils have low values of K due

to low runoff potential. However, because loamy soils are more likely to disintegrate and generate more runoff, their K values are higher [17]. The K values of the study area range from 0.1 to 1.1 $\text{Mg m}^2 \text{ h ha}^{-1} \text{ hJ}^{-1} \text{ cm}^{-1}$ (Figure 8a), the spatial distributions of the K factor in the research area. The color grey represents the lowest value of the K factor, while the color brown denotes high values of the K factor. Due to the closeness in climate, soil texture, and low values of SOM% [69], these results are consistent with those of other research conducted in similar dry valleys in Egypt and other regions in Saudi Arabia [95,96]. The slope length and gradient parameters are very important in the modeling of soil erosion [97]. The LS factor depends on slope length (L) and slope gradient (S), which are calculated from DEM values (Figure 8b) and range from 0 to 3.5. Steep locations had high LS values because the slope values were higher than those of the surrounding area [69]. This indicates that as slope length and slope steepness increase, soil loss will also increase; however, slope length has a greater impact on soil loss than slope steepness [16]. The findings showed that the R value, which is based on the amount of rain that produces soil erosivity, was 38.63. Vegetation cover is one of the most crucial factors in preventing soil erosion [79]. Thus, the S2A image was utilized to calculate the C factor of the investigated area according to the NDVI spatial distribution [69]. Typically, empirical equations are used to determine the vegetation factor [98]. However, the normalized difference vegetation index (NDVI) acquired by remote sensing technologies is the most widely used vegetation growth index, according to [99], and the results revealed that this index had a strong connection with ground biomass [100]. The soil adjusted vegetation index (SAVI) is the best VI (vegetation index), according to [101], for mapping soil erosion, while other indices such as NDVI, soil and atmospherically resistant vegetation index (SARVI) are also acceptable and relevant. Additionally, [102] highlighted the necessity of taking into account illumination conditions (IC) when interpreting vegetation indices (VI)_s over long time periods in order to boost the accuracy of monitoring VI in irregular topography. Nearly 50% of the study area is bare soil; therefore, the NDVI values are relatively low, ranging from 0.04 to 0.55 (Figure 8c). Values of NDVI 0–0.2 are considered to be bare soil, while the values from 0.2–0.7 are cultivated lands, and negative values are associated with water [103]. According to Figure 8d, the C factor ranges from 0.28–0.47; the agricultural areas have moderate values of C factor, while the highest values are found in the western part, where bare lands are located [104].

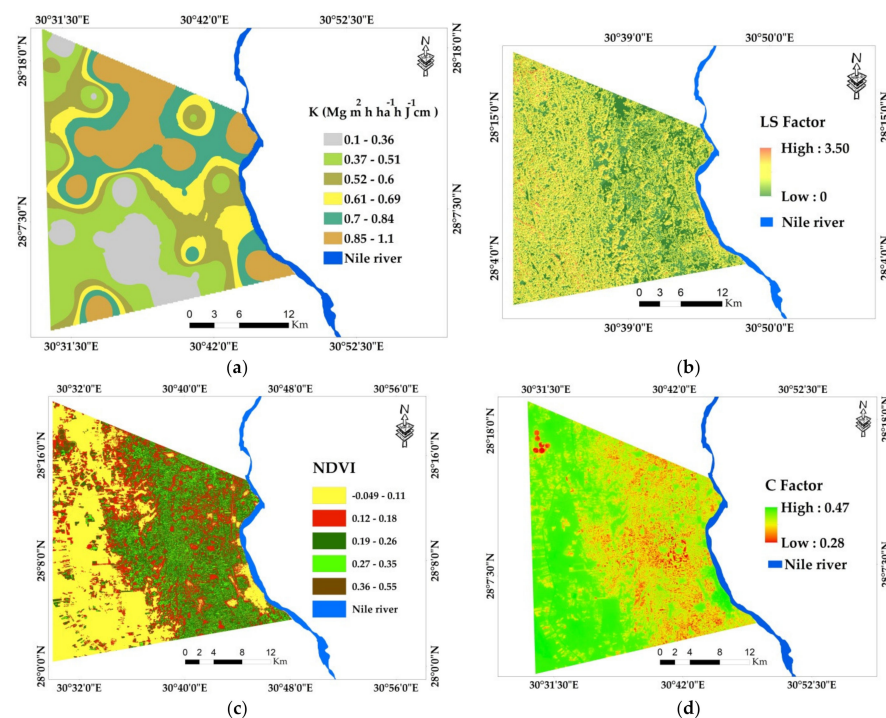


Figure 8. Spatial distribution of (a) k factor ($\text{t ha}^{-1} \text{ y}^{-1}$), (b) LS factor, (c) NDVI, and (d) C factor.

3.6. Estimation of Potential Soil Erosion and SWCR

To assess and show the spatial distribution of soil erosion within the area under investigation, the RS, GIS, and RUSLE models were merged. R K, L, S, C, and P factors were characterized as potential erosion factors. The annual erosion map of the research region is shown in Figure 9 as a consequence of the final soil loss model, which aids in identifying the areas that are vulnerable to soil erosion. The final soil erosion rate is affected by all five RUSLE factors; however, the effects on the erosion rate in this study are distinct. These characteristics fluctuate in different magnitudes, according to the analyses in this study. The yearly soil loss in the investigated area fluctuated between 0 and 28.67 t ha⁻¹ y⁻¹. As shown in Figure 9 and Table 4, around 29% of the study area is classified as being in the slight erosion class (<5 t ha⁻¹ y⁻¹), while 17.61% of the study area is characterized as being in the low erosion hazard class (5–10 t ha⁻¹ y⁻¹). The basins units (decantation and overflow basins) recognize these erosion classifications. The study area (23,312.7 ha) suffers from erosion at a moderate level (10–15 t ha⁻¹ y⁻¹); meanwhile, around 14,336 ha of the area under study are classified as having a moderately high erosion hazard (25–70 t ha⁻¹ y⁻¹) [104]. The high soil erosion values mean that these areas have a low ability to resist soil erosion, which may be due to several factors; for instance, low vegetation cover and high values of slope and other topographic features in the west of the study area. The pediments, shoulders, and peneplain units displayed the highest soil erosion hazards. The SWCR reflects the final and phased local soil and water conservation goals and the active process of realizing certain aims by soil and water conservation in a definite phase [105]. The current SWRC is 29.28%. It is obvious that several of the study’s western sections correspond to regions with moderately high potential for soil erosion. The findings of the present study could therefore be used to inform decision-makers about better soil management and land conservation. The required steps should be taken by public authorities to reduce the impact of these influencing characteristics.

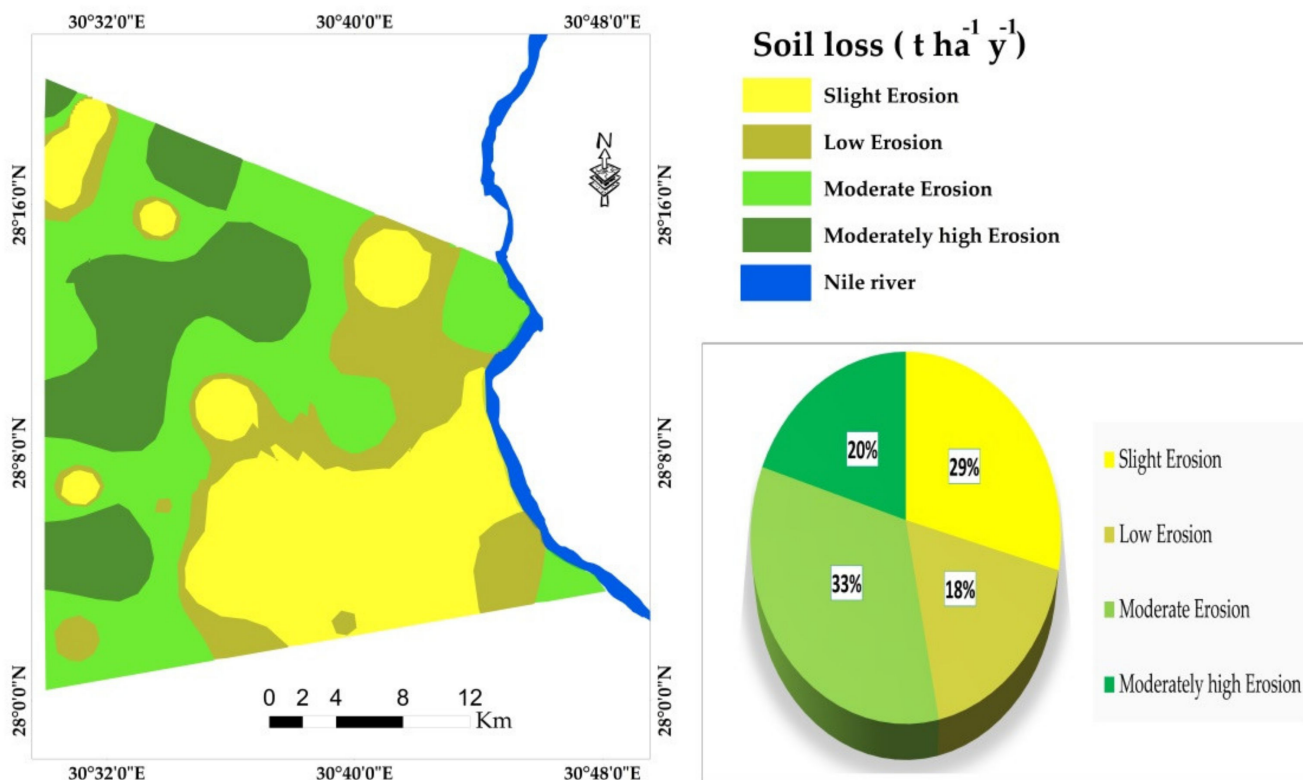


Figure 9. Spatial distribution of soil loss (t h⁻¹ y⁻¹) within investigated area and a pie chart representing the percent of soil erosion areas.

Table 4. Areas of soil loss over the study area.

Soil Loss Classes (t ha ⁻¹ y ⁻¹)	Area (ha)	Area (%)
Slight erosion	20,756.20	29.28
Low erosion	12,480.11	17.61
Moderate erosion	23,312.71	32.89
Moderately high erosion	14,336.15	20.22

4. Conclusions

Soil erosion risk assessment is key to sustainable agricultural development in arid regions, such as the El-Minya region of Egypt. This research uses the integration of RS, GIS, and the RUSLE model to estimate erosion rates in this region and was complemented with the SWCR model as a dynamic method to estimate the status of soil and water conservation practices in the study area. The advantages of RUSLE are its simplicity of use, the ease of interpretation of the data generated, and the fact that it is based on factors such as climate, topography, and soil properties that are manageable to map using GIS tools, are detectable by satellite remote sensing, and are interpretable through commonly used spectral indices. The results have allowed us to divide the study area into four relative classes of erosion: slight, low, moderate, and moderately high, whose spatial representation is intended to serve as a basis for the selective application of different soil management practices in order to minimize the effects of erosion. These practices include the protection of slopes and the increase in vegetation cover. In addition, it is proposed that SWCR be measured periodically, since it quantitatively measures the degree of soil control and water loss. Changes to the SWCR would allow a dynamic implementation of specific soil and water conservation practices. The results of the current study may help policymakers by providing management tools to remediate soil erosion in the study area and in similar arid regions under changing future scenarios.

Author Contributions: Conceptualization, E.A.A., M.A.A., F.O.H. and M.S.S.; methodology, E.A.A., M.A.A., F.O.H. and M.S.S.; software, E.A.A., M.A.A., F.O.H. and M.S.S.; validation, E.A.A., M.A.A., F.O.H. and M.S.S.; formal analysis, E.A.A., M.A.A., F.O.H. and M.S.S.; investigation, E.A.A., M.A.A., F.O.H. and M.S.S.; resources, E.A.A., M.A.A., F.O.H. and M.S.S.; data curation, E.A.A., M.A.A., F.O.H. and M.S.S.; writing—original draft preparation, E.A.A., M.A.A., F.O.H. and M.S.S.; writing—review and editing, M.S.S.; E.S.M.; A.A.E.B. and D.E.K. visualization, E.A.A., M.A.A., F.O.H. and M.S.S.; supervision, E.S.M.; A.A.E.B. and D.E.K. project administration, D.E.K.; funding acquisition, This research received no external funding. All authors have read and agreed to the published version of the manuscript.

Funding: This research received no external funding.

Institutional Review Board Statement: Not applicable.

Informed Consent Statement: Not applicable.

Data Availability Statement: Not applicable.

Acknowledgments: This paper was supported by the RUDN University Strategic Academic Leadership Program.

Conflicts of Interest: The authors declare no conflict of interest.

References

- Robinson, D.A.; Panagos, P.; Borrelli, P.; Jones, A.; Montanarella, L.; Tye, A.; Obst, C.G. Soil natural capital in Europe; a framework for state and change assessment. *Sci. Rep.* **2017**, *7*, 6706. [[CrossRef](#)] [[PubMed](#)]
- Keesstra, S.D.; Bouma, J.; Wallinga, J.; Tiftonell, P.; Smith, P.; Cerdà, A.; Montanarella, L.; Quinton, J.N.; Pachepsky, Y.; van der Putten, W.H. The significance of soils and soil science towards realization of the United Nations sustainable development goals. *Soil* **2016**, *2*, 111–128. [[CrossRef](#)]
- Amundson, R.; Berhe, A.A.; Hopmans, J.W.; Olson, C.; Sztein, A.E.; Sparks, D.L. Soil and human security in the 21st century. *Science* **2015**, *348*, 1261071. [[CrossRef](#)] [[PubMed](#)]

4. Kefi, M.; Yoshino, K.; Zayani, K.; Isoda, H. Estimation of soil loss by using combination of erosion model and GIS. Case study watersheds Tunis. *J. Arid Land Stud.* **2009**, *19*, 287–290.
5. Anache, J.A.A.; Bacchi, C.G.V.; Panachuki, E.; Sobrinho, T.A. Assessment of methods for predicting soil erodibility in soil loss modeling. *Geociências* **2016**, *34*, 32–40.
6. Sidi Almouctar, M.A.; Wu, Y.; Zhao, F.; Dossou, J.F. Soil erosion assessment using the rusle model and gwospatial techniques (remote sensing and gis) in South-Central Niger (Maradi Region). *Water* **2021**, *13*, 3511. [[CrossRef](#)]
7. Ping, Z.; Yajin, G.E.; JIANG, Y.; Yanan, X.I.E.; Zhiwen, S.I.; Hainan, Y.; Hong-Yuan, H.U.O.; Junchuan, Y.U.; Guanyuan, W.E.I. Assessment of soil erosion by the rusle model using remote sensing and gis: A case study of Jilin Province of China. *Environ. Sci.* **2020**, preprints.
8. Emadodin, I.; Bork, H. Degradation of soils as a result of long-term human-induced transformation of the environment in Iran: An overview. *J. Land Use Sci.* **2012**, *7*, 203–219. [[CrossRef](#)]
9. World Resources Institute. Available online: <https://www.wri.org/insights/causes-and-effects-soil-erosion-and-how-prevent-it> (accessed on 1 July 2022).
10. Regnier, P.; Friedlingstein, P.; Ciais, P.; Mackenzie, F.T.; Gruber, N.; Janssens, I.A.; Laruelle, G.G.; Lauerwald, R.; Luysaert, S.; Andersson, A.J.; et al. Anthropogenic perturbation of the carbon fluxes from land to ocean. *Nat. Geosci.* **2013**, *6*, 597–607. [[CrossRef](#)]
11. Tan, Z.; Leung, L.R.; Li, H.; Tesfa, T.; Zhu, Q.; Huang, M. A substantial role of soil erosion in the land carbon sink and its future changes. *Glob. Chang. Biol.* **2020**, *26*, 2642–2655. [[CrossRef](#)]
12. Ali, M.G.M.; Ahmed, M.; Ibrahim, M.M. Optimizing sowing window, cultivar choice, and plant density to boost maize yield under RCP8.5 climate scenario of CMIP5. *Int. J. Biometeorol.* **2022**, *66*, 971–985. [[CrossRef](#)]
13. Morgan, R.P.C. *Soil Erosion and Conservation*, 3rd ed.; Blackwell Publishing: Oxford, UK, 2005; p. 316.
14. Onyando, J.O.; Kisoyan, P.; Chemelil, M.C. Estimation of potential soil erosion for river perkerra catchment in Kenya. *Water Resour. Manag.* **2005**, *19*, 133–143. [[CrossRef](#)]
15. Abdel-Rahman, M.A.E.; Natarajan, A.; Hegde, R. Assessment of land suitability and capability by integrating remote sensing and GIS for agriculture in Chamarajanagar district, Karnataka, India. *Egypt. J. Remote Sens. Space Sci.* **2016**, *19*, 125–141.
16. Renard, K.G.; Foster, G.R.; Weesies, G.A.; McCool, D.K.; Yoder, D.C. *Predicting Soil Erosion by Water: A Guide to Conservation Planning with the Revised Universal Soil Loss Equation (RUSLE)*; United States Government Printing: Washington, DC, USA, 1997.
17. Prasannakumar, V.; Shiny, R.; Geetha, N.; Vijith, H. Spatial prediction of soil erosion risk by remote sensing, GIS and RUSLE approach: A case study of Siruvani river watershed in Attapady valley, Kerala, India. *Environ. Earth Sci.* **2011**, *64*, 965–972. [[CrossRef](#)]
18. Allafta, H.; Opp, C. Soil erosion assessment using the rusle model, remote sensing, and GIS in the Shatt Al-Arab basin (Iraq-Iran). *Appl. Sci.* **2022**, *12*, 7776. [[CrossRef](#)]
19. Ganasri, B.P.; Ramesh, H. Assessment of soil erosion by RUSLE model using remote sensing and GIS—A Case study of Nethravathi basin. *Geosci. Front.* **2016**, *7*, 953–961. [[CrossRef](#)]
20. Fu, B.; Wang, S.; Liu, Y.; Liu, J.; Liang, W.; Miao, C. Hydrogeomorphic ecosystem responses to natural and anthropogenic changes in the loess plateau of China. *Annu. Rev. Earth Planet. Sci.* **2017**, *45*, 223–243. [[CrossRef](#)]
21. Tadesse, L.; Suryabhagavan, K.V.; Sridhar, G.; Legesse, G. Land use and land cover changes and soil erosion in yezat watershed, north western Ethiopia. *Int. Soil Water Conserv. Res.* **2017**, *5*, 85–94. [[CrossRef](#)]
22. Sun, L.; Wan, S.; Luo, W. Biochars prepared from anaerobic digestion residue, palm bark, and eucalyptus for adsorption of cationic methylene blue dye: Characterization, equilibrium, and kinetic studies. *Bioresour. Technol.* **2013**, *140*, 406–413. [[CrossRef](#)]
23. Fan, J.R.; Zhang, J.H.; Zhong, X.H.; Liu, S.Z.; Tao, H.P. Monitoring of Soil Erosion and Assessment for Contribution of Sediments to Rivers in a Typical Watershed of the Upper Yangtze River Basin. *Land Degrad. Dev.* **2004**, *15*, 411–421. [[CrossRef](#)]
24. Pasquarella, V.J.; Holden, C.E.; Kaufman, L.; Woodcock, C.E. From imagery to ecology: Leveraging time series of all available Landsat observations to map and monitor ecosystem state and dynamics. *Remote Sens. Ecol. Conserv.* **2016**, *2*, 152–170. [[CrossRef](#)]
25. Young, N.E.; Anderson, R.S.; Chignell, S.M.; Vorster, A.G.; Lawrence, R.; Evangelista, P.H. A survival guide to Landsat preprocessing. *Ecology* **2017**, *98*, 920–932. [[CrossRef](#)] [[PubMed](#)]
26. Vaudour, E.; Gomez, Y.C.; Fouad, P. Lagacherie, Sentinel-2 image capacities to predict common topsoil properties of temperate and Mediterranean agroecosystems. *Remote Sens. Environ.* **2019**, *223*, 21–33. [[CrossRef](#)]
27. Lima, T.A.; Beuchle, R.; Langner, A.; Grecchi, R.C.; Griess, V.C.; Achard, F. Comparing Sentinel-2 MSI and Landsat 8 OLI Imagery for Monitoring Selective Logging in the Brazilian Amazon. *Remote Sens.* **2019**, *11*, 961. [[CrossRef](#)]
28. Ahady, A.B.; Kaplan, G. Classification comparison of Landsat-8 and Sentinel-2 data in Google Earth Engine, study case of the city of Kabul. *Int. J. Eng. Geosci.* **2022**, *7*, 24–31. [[CrossRef](#)]
29. Qin, Q.; Xu, D.; Hou, L.; Shen, B.; Xin, X. Comparing vegetation indices from Sentinel-2 and Landsat 8 under different vegetation gradients based on a controlled grazing experiment. *Ecol. Indic.* **2021**, *133*, 108363. [[CrossRef](#)]
30. Ayalew, D.A.; Deumlich, D.; Šarapatka, B.; Doktor, D. Quantifying the Sensitivity of NDVI-Based C Factor Estimation and Potential Soil Erosion Prediction using Spaceborne Earth Observation Data. *Remote Sens.* **2020**, *12*, 1136. [[CrossRef](#)]
31. Moravec, D.; Komárek, J.; López-Cuervo Medina, S.; Molina, I. Effect of Atmospheric Corrections on NDVI: Intercomparability of Landsat 8, Sentinel-2, and UAV Sensors. *Remote Sens.* **2021**, *13*, 3550. [[CrossRef](#)]

32. Huete, A.R.; Liu, H.Q. An error and sensitivity analysis of the atmosphere- and soil-correcting variants of the NDVI for the MODIS-EOS. *IEEE Trans. Geosci. Remote Sens.* **1994**, *32*, 897–905. [[CrossRef](#)]
33. Huete, A.R. A Soil Adjusted Vegetation Index (SAVI). *Remote Sens. Environ.* **1988**, *25*, 295–309. [[CrossRef](#)]
34. Kefi, M.; Yoshino, K.; City, T. Evaluation of the economic effects of soil erosion risk on agricultural productivity using remote sensing: Case of watershed in Tunisia. *Int. Arch. Photogramm. Remote. Sens. Spat. Inf. Sci.* **2010**, *38*, 930.
35. Yoshino, K.; Ishioka, Y. Guidelines for soil conservation towards integrated basin management for sustainable development: A new approach based on the assessment of soil loss risk using remote sensing and GIS. *Paddy Water Environ.* **2005**, *3*, 235–247. [[CrossRef](#)]
36. Hacısalihoğlu, S.; Oktan, E.; Yucesan, Z. Predicting Soil Erosion in Oriental Spruce (*Picea orientalis* (L.) Link.) Stands in Eastern Black Sea Region of Turkey. *Afr. J. Agric. Res.* **2010**, *5*, 2200–2214.
37. Leh, M.; Bajwa, S.; Chaubey, I. Impact of Land Use Change on Erosion Risk: An Integrated Remote Sensing, Geographic Information System and Modeling Methodology. *Land Degrad. Dev.* **2013**, *24*, 409–421. [[CrossRef](#)]
38. Lu, D.; Li, G.; Valladares, G.S.; Batistella, M. Mapping soil erosion risk in Rondonia, Brazilian Amazonia: Using RUSLE, remote sensing and GIS. *Land Degrad. Dev.* **2004**, *15*, 499–512. [[CrossRef](#)]
39. Bahadur, K. Mapping soil erosion susceptibility using remote sensing and GIS: A case of the Upper NamWa Watershed, Nan Province, Thailand. *Environ. Geol.* **2009**, *57*, 695–705. [[CrossRef](#)]
40. Perovic, V.; Zivotic, L.; Kadovic, R.; Dordevic, A.; Jaramaz, D.; Mrvic, V.; Todorovic, M. Spatial modelling of soil erosion potential in a mountainous watershed of South-eastern Serbia. *Environ. Earth Sci.* **2013**, *68*, 115–128. [[CrossRef](#)]
41. Pan, J.; Wen, Y. Estimation of soil erosion using RUSLE in Caijiamiao watershed. *China Nat. Hazards* **2014**, *71*, 2187–2205. [[CrossRef](#)]
42. Rawat, K.S.; Mishra, A.K.; Bhattacharyya, R. Soil erosion risk assessment and spatial mapping using landsat-7 ETM+, RUSLE, and GIS—A Case study. *Arab. J. Geosci.* **2016**, *9*, 288. [[CrossRef](#)]
43. Mayhoub, A.; Azzam, A. A survey on the assessment of wind energy potential in Egypt. *Renew. Energy* **1997**, *11*, 235–247. [[CrossRef](#)]
44. Hammam, A.A.; Mohamed, W.S.; Sayed, S.E.-E.; Kucher, D.E.; Mohamed, E.S. Assessment of soil contamination using gis and multi-variate analysis: A case study in El-Minia Governorate, Egypt. *Agronomy* **2022**, *12*, 1197. [[CrossRef](#)]
45. Malenovsky, Z.; Rott, H.; Cihlar, J.; Schaeppman, M.E.; García-Santos, G.; Fernandes, R.; Berger, M. Sentinels for science: Potential of Sentinel-1, -2, and -3 missions for scientific observations of ocean, cryosphere, and land. *Remote Sens. Environ.* **2012**, *120*, 91–101. [[CrossRef](#)]
46. Kaufman, Y.J.; Tanré, D.; Gordon, H.R.; Nakajima, T.; Lenoble, J.; Frouin, R.; Grassl, H.; Herman, B.M.; King, M.D.; Teillet, P.M. Passive Remote Sensing of Tropospheric Aerosol and Atmospheric Correction for the Aerosol Effect. *J. Geophys. Res. Space Phys.* **1997**, *102*, 16815–16830. [[CrossRef](#)]
47. Dobos, E.; Norman, B.; Worstell, B.; Al, E. The Use of DEM and Satellite Data for Regional Scale Soil Databases. *Agrokémia Talajt.* **2002**, *51*, 263–272. [[CrossRef](#)]
48. Felde, G.; Anderson, G.; Cooley, T.; Matthew, M.; Adler-Golden, S.; Berk, A.; Lee, J. Analysis of Hyperion Data with the FLAASH Atmospheric Correction Algorithm. In Proceedings of the 2003 IEEE International Geoscience and Remote Sensing Symposium, Toulouse, France, 21–25 July 2003; Volume 1, pp. 90–92.
49. Bui, Q.-T.; Jamet, C.; Vantrepotte, V.; Mériaux, X.; Cauvin, A.; Mognane, M.A. Evaluation of sentinel-2/msi atmospheric correction algorithms over two contrasted french coastal waters. *Remote Sens.* **2022**, *14*, 1099. [[CrossRef](#)]
50. Thapa, R.B.; Murayama, Y. Land evaluation for peri-urban agriculture using analytical hierarchical process and geographic information system techniques: A case study of Hanoi. *Land Use Policy* **2008**, *25*, 225–239. [[CrossRef](#)]
51. Chen, X.Y.; Chen, Y.; Wang, L.; Hu, Y.F. Text categorization based on frequent patterns with term frequency. In Proceedings of the Third International Conference on Machine Learning and Cybernetics, Shanghai, China, 26–29 August 2004.
52. Enderle, D.; Weih, R. Integrating supervised and unsupervised classification methods to develop a more accurate land cover classification. *J. Ark. Acad. Sci.* **2005**, *59*, 65–73.
53. Abdellatif, M.A.; El Baroudy, A.A.; Arshad, M.; Mahmoud, E.K.; Saleh, A.M.; Moghanm, F.S.; Shaltout, K.H.; Eid, E.M.; Shokr, M.S. A GIS-based approach for the quantitative assessment of soil quality and sustainable agriculture. *Sustainability* **2021**, *13*, 13438. [[CrossRef](#)]
54. Planchon, O.; Darboux, F. A fast, simple and versatile algorithm to fill the depressions of digital elevation models. *Catena* **2001**, *46*, 159–176. [[CrossRef](#)]
55. Dobos, E.; Daroussin, J.; Montanarella, L. *An SRTM-Based Procedure to Delineate SOTER Terrain Units on 1:1 and 1:5 Million Scales*; EUR 21571 EN; Office for Official Publications of the European Communities: Luxembourg, 2005; 55p.
56. Food and Agriculture Organization of the United Nations (FAO). *Guidelines for Soil Profile Description*, 3rd ed.; Food and Agriculture Organization of the United Nations: Rome, Italy, 2006.
57. Soil Survey Staff. *Keys to Soil Taxonomy*, USDA-NRCS, 11th ed.; U.S. Government Print Office: Washington, DC, USA, 2014.
58. Rhoades, J.D. Salinity: Electrical Conductivity and Total Dissolved Solids. In *Methods of Soil Analysis Part 3, Chemical Methods*; Sparks, D.L., Ed.; Soil Science Society of America Book Series, No. 5; Soil Science Society of America, American Society of Agronomy: Madison, WI, USA, 1996; pp. 417–435.

59. Thomas, G.W. Soil pH and Soil Acidity. In *Methods of Soil Analysis Part 3, Chemical Methods*; Sparks, D.L., Ed.; Soil Science Society of America Book Series, No. 5; Soil Science Society of America, American Society of Agronomy: Madison, WI, USA, 1996; pp. 475–490.
60. Summer, M.E.; Miller, W.P. Cation Exchange Capacity and Exchange Coefficients. In *Methods of Soil Analysis Part 3. Chemical Methods*; Sparks, D.L., Ed.; Soil Science Society of America Book Series, No. 5; Soil Science Society of America, American Society of Agronomy: Madison, WI, USA, 1996; pp. 1201–1229.
61. Lavkulich, L.M. *Methods Manual: Pedology Laboratory*; Department of Soil Science, University of British Columbia: Vancouver, BC, Canada, 1981.
62. Page, A.L.; Miller, R.H.; Keeney, D.R. *Methods of Soil Analysis (Part 2): Chemical and Microbiological Properties*, 2nd ed.; The American Society of Agronomy: Madison, WI, USA, 1982.
63. Wischmeier, W.H.; Smith, D.D. Predicting rainfall erosion losses. A guide to conservation planning. In *Agriculture Handbook*; US Department of Agriculture: Washington, DC, USA, 1978; Volume 537, p. 85.
64. Biswas, S.S.; Pani, P. Estimation of soil erosion using RUSLE and GIS techniques: A case study of Barakar River basin, Jharkhand, India. *Model. Earth Syst. Environ.* **2015**, *4*, 42. [[CrossRef](#)]
65. Thapa, P. Spatial estimation of soil erosion using rusle modeling: A case study of Dolakha District, Nepal. *Environ. Syst. Res.* **2020**, *9*, 15. [[CrossRef](#)]
66. Renard, K.G.; Freimund, J.R. Using monthly precipitation data to estimate the R-factor in the revised USLE. *J. Hydrol.* **1994**, *157*, 287–306. [[CrossRef](#)]
67. Parysow, P.; Wang, G.X.; Gertner, G.; Anderson, A.B. Spatial uncertainty analysis for mapping soil erodibility based on joint sequential simulation. *Catena* **2003**, *53*, 65–78. [[CrossRef](#)]
68. Gelagay, H.S.; Minale, A.S. Soil loss estimation using GIS and remote sensing techniques: A case of Koga watershed, Northwestern Ethiopia. *Int. Soil Water Cons. Res.* **2016**, *4*, 126–136. [[CrossRef](#)]
69. Azab, Y.F.A.; Abbas, H.H.; Jalhoun, M.E.M.; Farid, I.M.; Abdelhameed, A.H.; Mohamed, E.S. Soil erosion assessment in arid region: A case study in Wadi Naghamish, Northwest Coast, Egypt. *Egypt. J. Rem. Sens. Space Sci.* **2021**, *24*, 1111–1118. [[CrossRef](#)]
70. Tucker, C.J. Use of Near Infrared/Red Radiance Ratios for Estimating Vegetation Biomass and Physiological Status NASA Technical Report. 1977, X-923-77-183. p. 41. Available online: <https://ntrs.nasa.gov/citations/19770025621> (accessed on 3 September 2013).
71. Farhan, Y.; Nawaiseh, S. Spatial assessment of soil erosion risk using RUSLE and GIS techniques. *Environ. Earth Sci.* **2015**, *74*, 4649–4669. [[CrossRef](#)]
72. Diwediga, B.; Le, Q.B.; Agodzo, S.K.; Tamene, L.D.; Wala, K. Modelling Soil Erosion Response to Sustainable landscape management scenarios in the Mo River basin (Togo, West Africa). *Sci. Total Environ.* **2018**, *625*, 1309–1320. [[CrossRef](#)]
73. Pu, C.Y. Scientific determination and application of soil and water conservation rate. *Soil Water Conserv. China* **2021**, 1–3. [[CrossRef](#)]
74. Goovaerts, P. *Geostatistics for Natural Resource Evaluation*; Oxford University Press: Oxford, UK, 1997.
75. Korhonen, L.; Packalen, P.; Rautiainen, M. Comparison of Sentinel-2 and Landsat 8 in the estimation of boreal forest canopy cover and leaf area index. *Remote Sens. Environ.* **2017**, *195*, 259–274. [[CrossRef](#)]
76. García-Llamas, P.; Suárez-Seoane, S.; Fernández-Guisuraga, J.M.; Fernández-García, V.; Fernández-Manso, A.; Quintano, C.; Calvo, L. Evaluation and comparison of Landsat 8, Sentinel-2 and Deimos-1 remote sensing indices for assessing burn severity in Mediterranean fire-prone ecosystems. *Int. J. Appl. Earth Obs. Geoinf.* **2019**, *80*, 137–144.
77. Wang, J.; Ding, J.; Yu, D.; Teng, D.; He, B.; Chen, X.; Yang, X. Machine learning-based detection of soil salinity in an arid desert region, Northwest China: A comparison between Landsat-8 OLI and Sentinel-2 MSI. *Sci. Total Environ.* **2020**, *707*, 136092. [[CrossRef](#)] [[PubMed](#)]
78. Henry, P. Levees and other raised ground. *Am. Sci.* **2006**, *94*, 7–11.
79. Schoeneberger, P.J.; Wysocki, D.A.; National Soil Survey Center, NRCS, Lincoln, NE, USA. Personal communication, 2013.
80. Oldknow, C.J.; Hooke, J.M. Alluvial terrace development and changing landscape connectivity in the Great Karoo, South Africa. Insights from the Wilgerbosch River catchment, Sneeuwberg. *Geomorphology* **2017**, *288*, 12–38. [[CrossRef](#)]
81. Hawley, J.W.; Parsons, R.B. *Glossary of Selected Geomorphic and Geologic Terms*; Mimeo; USDA Soil Conservation Service, West National Technical Center: Portland, OR, USA, 1980; 30p.
82. Ruhe, R.V. *Geomorphology: Geomorphic Processes and Surficial Geology*; Houghton-Mifflin: Boston, MA, USA, 1975; 246p.
83. Ali, R.R.; Moghanm, F.S. Variation of soil properties over the landforms around Idku lake, Egypt. *Egypt. J. Remote Sens. Space Sci.* **2013**, *16*, 91–101. [[CrossRef](#)]
84. Baruah, T.; Barthakur, H.A. *Textbook of Soil Analysis*; Vikas Publishing House PVT Ltd.: New Delhi, India, 1997.
85. Neina, D. The role of soil pH in plant nutrition and soil remediation. *Appl. Environ. Soil Sci.* **2019**, *2009*, 5794869. [[CrossRef](#)]
86. Brady, N.C.; Weil, R.R.; Weil, R.R. *The Nature and Properties of Soils*; Prentice Hall: Upper Saddle River, NJ, USA, 2008; Volume 13.
87. Nachshon, U. Cropland soil salinization and associated hydrology: Trends, processes and examples. *Water* **2018**, *10*, 1030. [[CrossRef](#)]
88. Zalacáin, D.; Martínez-Pérez, S.; Bienes, R.; García-Díaz, A.; Sastre-Merlín, A. Salt accumulation in soils and plants under reclaimed water irrigation in urban parks of Madrid (Spain). *Agric. Water Manag.* **2019**, *213*, 468–476. [[CrossRef](#)]

89. El-Behairy, R.A.; El Baroudy, A.A.; Ibrahim, M.M.; Kheir, A.M.S.; Shokr, M.S. Modelling and assessment of irrigation water quality index using GIS in semi-arid region for sustainable agriculture. *Water Air Soil Pollut.* **2021**, *232*, 352. [[CrossRef](#)]
90. Abdel-Fattah, M.K.; Mohamed, E.S.; Wagdi, E.M.; Shahin, S.A.; Aldosari, A.A.; Lasaponara, R.; Alnaimy, M.A. Quantitative evaluation of soil quality using principal component analysis: The case study of El-Fayoum Depression Egypt. *Sustainability* **2021**, *13*, 1824. [[CrossRef](#)]
91. Shokr, M.S.; Abdellatif, M.A.; El Baroudy, A.A.; Elnashar, A.; Ali, E.F.; Belal, A.A.; Attia, W.; Ahmed, M.; Aldosari, A.A.; Szantoi, Z. Development of a Spatial model for soil quality assessment under arid and semi-arid conditions. *Sustainability* **2021**, *13*, 2893. [[CrossRef](#)]
92. Mohamed, E.S.; Baroudy, A.A.E.; El-beshbeshy, T.; Emam, M.; Belal, A.A.; Elfadaly, A.; Aldosari, A.A.; Ali, A.M.; Lasaponara, R. Vis-NIR Spectroscopy and Satellite Landsat-8 OLI data to map soil nutrients in arid conditions: A case study of the Northwest Coast of Egypt. *Remote Sens.* **2020**, *12*, 3716. [[CrossRef](#)]
93. Abd-Elmabod, S.K.; Mansour, H.; Hussein, A.; Mohamed, E.S.; Zhang, Z.; Anaya-Romero, M.; Jordán, A. Influence of irrigation water quantity on the land capability classification. *Plant Arch.* **2019**, *2*, 2253.
94. Shokr, M.S.; Mazrou, Y.S.A.; Abdellatif, M.A.; El Baroudy, A.A.; Mahmoud, E.K.; Saleh, A.M.; Belal, A.A.; Ding, Z. Integration of Geostatistical and sentinel-2 multispectral satellite image analysis for predicting soil fertility condition in drylands. *ISPRS Int. J. Geo-Inf.* **2022**, *11*, 353. [[CrossRef](#)]
95. Kawy, W.A.; El-Nady, M.A. Soil erosion assessment using revised universal soil loss equation for selective dry valleys in the eastern desert of Egypt. *Aust. J. Basic Appl. Sci.* **2009**, *3*, 836–843.
96. Bahrawi, J.A.; Elhag, M.; Aldhebiani, A.Y.; Galal, H.K.; Hegazy, A.K.; Alghailani, E. Soil erosion estimation using remote sensing techniques in Wadi Yalamlam Basin, Saudi Arabia. *Adv. Mater. Sci. Eng.* **2016**, *2016*, 9585962. [[CrossRef](#)]
97. Morgan, R.P.C.; Morgan, D.D.V.; Finney, H.J. A predictive model for the assessment of soil erosion risk. *J. Agric. Eng. Res.* **1984**, *30*, 245–253. [[CrossRef](#)]
98. Liu, H.; Zhao, W.; Liu, Y. Assessment on the Soil retention service of water Erosion in the Nile River Basin considering vegetation factor variance from 1982 to 2013. *Water* **2020**, *12*, 2018. [[CrossRef](#)]
99. Lin, C.Y. A study on the width and placement of vegetated buffer strips in a mudstone-distributed watershed. *J. China Soil Water Conserves* **1997**, *29*, 250–266, (In Chinese with English abstract).
100. Fathizad, H.; Karimi, H.; Alibakhshi, S.M. The estimation of erosion and sediment by using the RUSLE model and RS and GIS techniques (case study: Arid and semi-arid regions of Doviraj, Ilam province, Iran). *Int. J. Agric. Crop Sci. (IJACS)* **2014**, *7*, 304–314.
101. Phinzi, K.; Ngetar, N. Mapping soil erosion in a quaternary catchment in Eastern Cape using geographic information system and remote sensing. *S. Afr. J. Geomat.* **2017**, *6*, 11–29. [[CrossRef](#)]
102. Martín-Ortega, P.; García-Montero, L.G.; Sibelet, N. Temporal Patterns in Illumination Conditions and Its Effect on Vegetation Indices Using Landsat on Google Earth Engine. *Remote Sens.* **2020**, *12*, 211. [[CrossRef](#)]
103. Linage, S. *Quantitative Remote Sensing of Land Surface*; Wiley: New Jersey, NJ, USA, 2004; pp. 479–501.
104. Bera, A. Estimation of soil loss by USLE model using gis and remote sensing techniques: A case study of Muhuri River basin, Tripura, India. *Eurasian J. Soil Sci.* **2017**, *6*, 206–215. [[CrossRef](#)]
105. Fang, F.; Fang, Q.; Yu, W.; Fan, C.; Zi, R.; Zhao, L. RUSLE model evaluation of the soil and water conservation ratio of the guizhou province in china between 2000 and 2019. *Sustainability* **2022**, *14*, 8219. [[CrossRef](#)]

Disclaimer/Publisher’s Note: The statements, opinions and data contained in all publications are solely those of the individual author(s) and contributor(s) and not of MDPI and/or the editor(s). MDPI and/or the editor(s) disclaim responsibility for any injury to people or property resulting from any ideas, methods, instructions or products referred to in the content.